

4D MRI Flow Coupled to Physics-Based Fluid Simulation for Blood-Flow Visualization

N. de Hoon¹, R. van Pelt², A. Jalba¹, and A. Vilanova^{2,3}

¹Computer Science and Mathematics, Eindhoven University of Technology, The Netherlands

²Biomedical Engineering, Eindhoven University of Technology, The Netherlands

³Electrical Engineering, Mathematics and Computer Science, Delft University of Technology, The Netherlands

Abstract

Modern MRI measurements deliver volumetric and time-varying blood-flow data of unprecedented quality. Visual analysis of these data potentially leads to a better diagnosis and risk assessment of various cardiovascular diseases. Recent advances have improved the speed and quality of the imaging data considerably. Nevertheless, the data remains compromised by noise and a lack of spatiotemporal resolution. Besides imaging data, also numerical simulations are employed. These are based on mathematical models of specific features of physical reality. However, these models require realistic parameters and boundary conditions based on measurements. We propose to use data assimilation to bring measured data and physically-based simulation together, and to harness the mutual benefits. The accuracy and noise robustness of the coupled approach is validated using an analytic flow field. Furthermore, we present a comparative visualization that conveys the differences between using conventional interpolation and our coupled approach.

Categories and Subject Descriptors (according to ACM CCS): I.3.8 [Computer Graphics]: Applications—4D PC-MRI Blood-Flow I.6.8 [Simulation and Modeling]: Types of Simulation—Combined G.1.1 [Mathematics of Computing]: Numerical Analysis—Interpolation

1. Introduction

Traditional diagnosis and risk assessment of cardiovascular disease relies on morphological information found in anatomical medical imaging data. However, blood-flow data also contain valuable information to aid the assessment of cardiovascular disease, which is currently the leading cause of death worldwide with more than a third of the deaths in the United States [GMR*13]. A large body of clinical research indicates that atypical blood flow affects disease development [MFK*12]. The anomalous blood-flow influences the cardiovascular morphology, and in turn small morphological changes alter the hemodynamics.

Contemporary imaging modalities, such as Doppler ultrasound and phase-contrast magnetic resonance imaging (PC-MRI), enable acquisition of blood-flow velocity data. While other modalities are more cost effective, PC-MRI provides unsurpassed quality volumetric velocity data throughout a heartbeat. We use reconstructed data directly from the scanner, without further processing, as shown in Fig. 1. Our acquisition typically consists of 20 to 25 phases that cover a

heartbeat, with a temporal resolution of about 40ms. Each phase in the series consists of a vector volume containing about $150 \times 150 \times 50$ voxels, sized $2.0 \times 2.0 \times 2.5$ mm. Acquisition was performed with a velocity encoding (venc) speed of 2 m/s, repetition time (TR) 4.7ms, echo time (TE) 2.7ms, and a flip angle of 5° . Our measurements have a $SNR \approx 10$. An overview of the acquisition and applications of these 4D blood-flow data is given by Markl et al. [MFK*12].

These imaging data provide important patient-specific information, typically capturing the thoracic arteries and heart chambers. However, they are prone to noise and artifacts, which impair the analysis. Besides phase-wrap artifacts, which are often corrected by tailored algorithms, motion artifacts occur especially in the vicinity of the moving cardiac and vessel walls. Also, the spatial resolution remains limited, leading to partial volume effects. This causes poorly defined velocity vectors near the walls, because boundary transitions occur at sub-voxel scale. The most pressing issue for the analysis is, however, the coarse temporal resolution.

We aim to make good use of the temporal resolution achievable with modern 4D flow imaging. To date most blood-flow visualizations employ linear interpolation to approximate values between the coarsely spaced time points. Many visualization techniques, such as line and particle traces, rely on numerical integration methods that use interpolated values. Physical knowledge about the blood-flow behavior is currently not employed to improve the approximation of inter-measurement velocity information, even though this knowledge is well established in literature. The field of fluid dynamics studies the physical aspects of fluid flow, providing a variety of computational methods to model the unsteady flow behavior. These simulations result in high-resolution and noise-free models of the fluid dynamics. However, these simulations approximate the actual fluid motion, and rely on a number of model assumptions. These assumptions are necessary to reduce computational complexity, but can also be specific to the domain. For blood-flow simulations, the results depend heavily on the quality of the vessel wall segmentation, and the measured in- and outflow conditions. Consequently, reliable patient-specific results are hard to achieve, and simulations are therefore still scarcely used in clinical practice.

To harness the advantages of both blood-flow measurements and simulations, we advocate for a viewpoint where both approaches are coupled, through the generic technique of data assimilation (DA) – the process of combining governing principles with potentially sparse, noisy and/or irregularly-distributed data. The DA technique is well established in fields such as geophysics and meteorology, where sparse and noisy data are combined with dynamics principles to obtain accurate predictions of physical phenomena, see e.g., Ghil and Malanotte [GMR91]. Here, we propose such an approach that enriches the full 4D measured velocity data using physics-based simulation. In contrast to current simulation techniques, which merely take in- and outflow conditions, the full 4D blood-flow data is used to steer the simulation.

Instead of the conventional computational fluid dynamics (CFD) approaches, which mostly rely on computationally expensive finite-element models, we incorporate a fluid dynamics method that stems from computer graphics research. Such methods, typically used for movies and games, provide an unmatched computational performance, and are nowadays typically based on physical knowledge, modeling the incompressible fluid in a well-defined boundary, while conserving mass and energy. In particular, we use a hybrid fluid simulation, combining a grid-based and particle-based approach. This results in a fast and feature-preserving simulation, providing a better accuracy considering the resolution of the measured data. Moreover, the coupling eliminates measurement noise and artifacts.

In summary, the main contributions of this paper are:

- a novel coupling approach between 4D PC-MRI blood-



Figure 1: Example of a 4D PC-MRI blood-flow dataset. Three slices depict the velocity components at 200ms.

flow measurements and fluid simulations, enabling a physics-based temporal interpolation, and a reduction of acquisition noise and artifacts;

- a validation of the coupling approach, assessing the accuracy of inter-measurement velocities and noise robustness using synthetic flow data as ground truth;
- a comparative flow visualization using pathlines, conveying the difference between conventional interpolation and our coupled approach, for healthy and pathological data.

2. Related work

Understanding the blood-flow behavior can aid the diagnosis and prognosis of pathology, as well as the assessment of treatment risk and follow-up findings for cardiovascular diseases [MFK*12]. Besides quantitative analyses, comprehensive visualization is essential to gain understanding of the intricate blood-flow patterns in relation to disease development [VPvP*12]. Recent advances show that integral line visualizations can be filtered to produce an effective representation of the blood-flow dynamics [BMGS13, KGP*13].

These visualization techniques employ numerical methods, e.g., Runge-Kutta integration, to trace blood-flow trajectories. Most methods therefore employ linear interpolation to cope with the limited temporal resolution, and hence rely on rough inter-measurement approximations. Alternatively, Schwenke et al. proposed an anisotropic fast marching approach, modeling the blood-flow trajectories as minimal paths between time points [SHFF11]. Although their approach considers accumulated uncertainty in the trajectories, they do not take physical laws into account.

We present a novel approach using the full 4D MRI blood-flow measurements, coupled with a physics-based simulation. Contrary to common CFD-based modeling [TF09], we employ fluid simulations from the field of computer graphics. Although the accuracy is generally inferior to CFD techniques, the methods are fast and rely on fluid physics. Fluid simulation techniques are divided into grid-based and particle-based approaches, respectively referred to as Eulerian and Lagrangian methods.

In his seminal work, Stam presented a stable semi-Lagrangian fluid simulation with regard to advection, enforcing incompressibility and mass conservation using a Eulerian grid representation [Sta99]. However, Eule-

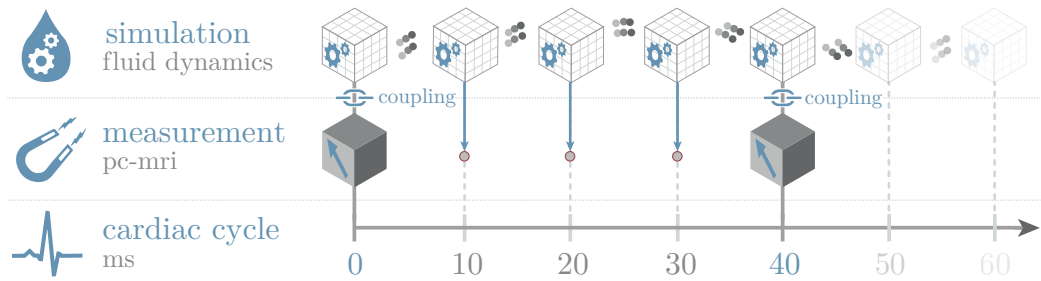


Figure 2: Overview of the measurement-simulation coupling. The 4D PC-MRI data is represented by cubes with an arrow. We propose a coupled approach between the full measured data and hybrid fluid simulation, represented by grids and particles. For each time point of the cardiac cycle at which MRI data exists, the simulation is coupled with the measurements. In-between measurements, the simulation provides physics-based interpolated velocity fields, e.g., on the positions of the red dots.

rian approaches lack details in regions with high vorticity. Lagrangian techniques exhibit more small-scale features, since they model fluids using particles. Examples are the ‘smoothed particle hydrodynamics’ (SPH) method [MCG03] and the ‘vortex particle method’ [SRF05]. Incompressibility is, however, hard to ensure. To exploit the best of both the Eulerian and Lagrangian approaches, hybrid simulation techniques have been proposed, using both particles and grids. In this work, we largely adopt the widely used ‘fluid implicit particle’ (FLIP) method, introduced by Brackbill et al. [BKR88]. This hybrid approach preserves details and ensures incompressibility.

To make the coupling between measurement and simulation, we need to control the fluid simulation. Such controllability is often employed by animators to produce various effects [FM97], for instance using a potential field to steer the fluid [HK04]. Such controllability can be used to guide the fluid simulations closer to the measured velocity fields.

To date, the measured data are mostly used as inflow condition for simulations [WWK*01], or deployed to evaluate the simulation outcome [GWV*02]. One approach that couples the full imaging data with a simulation was proposed by Funamoto et al. [FHS*05]. The authors aim to reduce acquisition artifacts by integrating 2D Doppler ultrasound data with a fluid simulation, steering the results with a feedback signal based on the difference between the measurement and simulation. Recently, D’Elia et al. [DPV12] proposed a DA-based technique, including noisy velocity measurements into fluid simulations for hemodynamics applications. Their approach relies on finite elements to discretize the steady Navier-Stokes equations on irregular domains. The coupling is done within the context of variational DA, formulating the problem as the minimization of the squared difference of the measured and simulated velocities, subject to equality constraints required to enforce boundary and incompressibility conditions. The resulting non-linear constrained optimization is solved using Newton iteration.

In this work, we adopt a similar line of reasoning, coupling the full 4D blood-flow data with an unsteady fluid sim-

ulation, based on the fast FLIP method. Besides a reduction of measurement artifacts, we have tailored our method to address the limited temporal resolution of the MRI data. Although our coupling scheme could be seen as a simplified version of the variational method of D’Elia et al. [DPV12], we focus on unsteady volumetric blood flow, and not on 2D steady flows.

3. Coupling measurements with simulation

3.1. Blood-flow Simulation

We model blood as an incompressible, inviscid fluid based on the Navier-Stokes equations, given by

$$\begin{cases} \frac{\partial \mathbf{u}}{\partial t} = -\mathbf{u} \cdot \nabla \mathbf{u} - \frac{1}{\rho} \nabla p \\ \nabla \cdot \mathbf{u} = 0, \end{cases} \quad (1)$$

where \mathbf{u} is the fluid velocity, p is the pressure and ρ is the density. Since the divergence ($\nabla \cdot \mathbf{u}$) measures the rate of change of the fluid per unit volume, the second equation above enforces incompressibility of the blood flow.

Note that for simplicity, we model blood as an inviscid fluid, thus initially neglecting its viscosity. However, in Section 6 we show initial results where viscous effects are taken into account. Although it is common to neglect viscosity when simulating water for computer graphics applications [Bri08], our choice of excluding viscosity was also based on the inherent numerical viscosity, as well as domain-specific characteristics; e.g., unreliable location of the vessel walls and the fact that viscosity effects are minimal at high-speed blood flow through the main vessels. Whereas the ‘no-slip condition’ is generally used for modeling viscous flows, here we use the ‘no-penetration condition’, i.e., $\mathbf{u} \cdot \hat{\mathbf{n}} = \mathbf{v}_{wall} \cdot \hat{\mathbf{n}} = 0$, with $\hat{\mathbf{n}}$ and \mathbf{v}_{wall} being the unit normal and velocity of the solid vessel boundary, respectively; additionally we assume $\mathbf{v}_{wall} = 0$ (static walls). Thus, the blood velocity normal to the vessel wall is set to zero, whereas the velocity parallel to the wall is unaffected. This is in accordance with our inviscid-flow modeling choice, where the effect of boundary layers is neglected.

Algorithm 1: Blood-flow simulation algorithm.

```

1 Initialize positions and velocities of FLIP particles;
2 foreach simulation time step do
3   Compute velocity of each grid cell as a weighted average
   of nearby particle velocities;
4   Advect particles through the grid velocity field using a
   second-order Runge-Kutta ODE solver; also, constrain
   particles to lie inside vessel walls;
5   Extend fluid-cell velocities to nearby non-fluid cells;
6   Make the grid velocity incompressible;
7   Add to particle velocities the differences between grid
   velocities at steps 3 and 6;
8   Create new FLIP particles;
9 end

```

The initial velocity, \mathbf{u}^0 , is set to the first MRI flow measurement. We use a standard operator-splitting approach that allows separating the right-hand components of Eq. (1) into multiple terms, calculated in sequence, independently of one another. First we account for the $\mathbf{u} \cdot \nabla \mathbf{u}$ term by advecting \mathbf{u}^n , the current, incompressible velocity field, forward in time with the FLIP method [BKR88], yielding an advected velocity \mathbf{u}^* . Thus, the advection PDE $\partial \mathbf{u} / \partial t = -\mathbf{u} \cdot \nabla \mathbf{u}$ is discretized in time via

$$\frac{\mathbf{u}^* - \mathbf{u}^n}{\Delta t} = -\mathbf{u}^n \cdot \nabla \mathbf{u}^n.$$

Then, for the pressure term, \mathbf{u}^* is made incompressible using the method by Batty et al. [BBB07], while also taking into account boundary conditions. Accordingly, the following (sparse) linear system is solved using an (incomplete) Cholesky-preconditioned Conjugate Gradient solver

$$\frac{\Delta t}{\rho^2} \mathbf{G}^T \mathbf{M} \mathbf{G} \mathbf{p}^{n+1} = \frac{1}{\rho} \mathbf{G}^T \mathbf{M} \mathbf{u}^*, \quad (2)$$

with \mathbf{G} a finite-difference gradient operator, \mathbf{M} the diagonal matrix of all fluid-cell masses and \mathbf{p}^{n+1} the vector of unknown pressure values. Once the pressure field is obtained, it is applied via

$$\mathbf{u}^{n+1} = \mathbf{u}^* - \frac{\Delta t}{\rho} \mathbf{G} \mathbf{p}^{n+1}. \quad (3)$$

The equations above are discretized on a so-called staggered MAC grid, enabling simple and stable pressure solvers. On the MAC grid, fluid velocities are stored component-wise on cell faces, whereas pressure values are stored at cell centers. We rely on the FLIP method to perform the advection step. The FLIP method is a hybrid, Lagrangian-Eulerian approach that uses both particles and an auxiliary grid to achieve good preservation of small-scale features and low numerical dissipation. Within FLIP, particles constitute the fundamental representation of the fluid, whereas the grid is used to merely modify particle values due to the pressure term; see Zhu et al. [ZB05] for more details.

The main steps of our blood-flow simulation are shown in Alg. 1. During the simulation, new FLIP particles are created in empty (non-fluid) grid cells surrounding non-empty

(fluid) ones, step 8. By the CFL condition empty cells can only occur next to non-empty ones, since the fluid cannot move more than one grid cell per time step. The velocity at these cells is initialized by extending the velocity field of the fluid using the Fast Sweeping Method [Zha05], see step 5 of Alg. 1. The new particles get their velocities from the grid cells they occupy, by using an approach similar to SPH interpolation [GM77]. If a measurement is available at the current time step, the measured velocity field is used instead of the simulation field. The density field ρ is evaluated on the grid using SPH interpolation of particles' masses. In step 6, the grid velocity is made incompressible using the variational method by Batty et al. [BBB07]. One advantage of this method is that it avoids *locally* discretizing the sensitive boundary condition $\mathbf{u} \cdot \hat{\mathbf{n}} = 0$, employed by standard pressure PDE solvers at non-grid-aligned vessel walls. Instead it solves the normal equations for pressure – a *global*, consistent, symmetric positive semi-definite system given in Eq. (2). Fluid-cell masses, giving the weights in Eq. (2), are estimated using a volume-of-fluid approach at non-grid-aligned vessel walls. More implementation details are given by Batty et al. [BBB07].

3.2. Coupling

An overview of our measurement-simulation coupling scheme is provided in Fig. 2. Let \mathbf{u} be the simulation velocity field, \mathbf{u}_m denote the measured velocity field, and let $\mathbf{u}_d \equiv \mathbf{u} - \mathbf{u}_m$ be the velocity difference between simulation and measurements. Thus, ideally, in the absence of noise, $\mathbf{u}_d = 0$. The main idea of our coupling scheme is to construct the new simulation velocity field \mathbf{u}^{new} at discrete time step $n+1$ as $\mathbf{u}^{new} \leftarrow \mathbf{u}^{n+1} - \gamma \mathbf{u}_d^{n+1}$, with γ a weight parameter and both fields \mathbf{u}^{n+1} and \mathbf{u}_d^{n+1} divergence-free, i.e., $\nabla \cdot \mathbf{u}^{n+1} = \nabla \cdot \mathbf{u}_d^{n+1} = 0$, see above. Although parameter γ can be used to bias selectively the resulting velocity field towards simulation ($\gamma = 0$) or measurement ($\gamma = 1$) across the time steps, we fix its value and use $\gamma = 1$. Note that the term $\gamma \mathbf{u}_d^{n+1}$ can also be interpreted as a spring force (or similarity term) with stiffness γ , keeping the simulation velocity field close to the measurement.

Since the measurement field represents blood-flow velocity samples in the main arteries, we assume that it also obeys the momentum-conservation law of the Navier-Stokes equations, i.e.,

$$\frac{\partial \mathbf{u}_m}{\partial t} = -\mathbf{u}_m \cdot \nabla \mathbf{u}_m. \quad (4)$$

However, \mathbf{u}_m may not be divergence-free, due to noise corruption and other scanning artifacts. Thus, unlike in Eq. (1), we omit in Eq. (4) the pressure term, enforcing fluid incompressibility. Subtracting Eq. (4) from the corresponding Eq. (1), one obtains

$$\frac{\partial \mathbf{u}_d}{\partial t} = -\mathbf{u} \cdot \nabla \mathbf{u} + \mathbf{u}_m \cdot \nabla \mathbf{u}_m - \frac{1}{\rho} \nabla p. \quad (5)$$

Algorithm 2: Measurement-simulation coupling.

- 1 Store current \mathbf{u}^n on the grid, see step 3 of Alg. 1; the measured velocity \mathbf{u}_m^n already comes on a grid;
- 2 Advect FLIP particles independently using \mathbf{u}^n and \mathbf{u}_m^n , see step 4 of Alg. 1;
- 3 Given \mathbf{u}^* and \mathbf{u}_m^* , evaluate \mathbf{u}_d^* on a grid;
- 4 Extend \mathbf{u}_d^* and make it incompressible, see steps 5 and 6 of Alg. 1;
- 5 Extend \mathbf{u}^* and make it incompressible;
- 6 Perform step 7 of Alg. 1 and store velocities \mathbf{u}^{n+1} and \mathbf{u}_d^{n+1} in the FLIP particles;
- 7 Set new simulation velocity using $\mathbf{u}^{new} \leftarrow \mathbf{u}^{n+1} - \mathbf{u}_d^{n+1}$;

Similar to Eq. (1), we rely on operator splitting to separate the advective and pressure terms from Eq. (5). First we account for the $-\mathbf{u} \cdot \nabla \mathbf{u} + \mathbf{u}_m \cdot \nabla \mathbf{u}_m$ terms by advecting \mathbf{u} and \mathbf{u}_m forward in time using the FLIP scheme, giving a velocity difference \mathbf{u}_d^* . This velocity field is then made incompressible, similar to Eq. (2), using the method by Batty et al. [BBB07]. Once the pressure field is obtained, the Helmholtz-Hodge decomposition, or alternatively Eq. (3), allows us to obtain the divergence-free field \mathbf{u}_d^{n+1} . To summarize, the main steps of our coupling scheme, applied whenever new measured velocities are available, are given in Alg. 2. For the time steps when no measured data are available, the standard simulation algorithm, Alg 1, is used. The simulation grid size is set to the size of the input volumes containing velocity measurements.

4. Evaluation

We present several experiments to assess the accuracy and robustness of the proposed coupling approach.

4.1. Experiment Setup

Validation of PC-MRI methods is difficult mainly due to the lack of ground truth. There is no analytical description for unsteady flows that goes beyond a simple pulsatile example in a straight tube [THZ98]. Therefore, the generation of realistic synthetic data remains challenging. However, interesting general characteristics of the tested methods can still be analyzed using such fields. The used synthetic data here consist of a parametric flow field describing a rotational vortex. The velocity $\mathbf{v} = (u, v, w)$ at position $\mathbf{x} = (x, y, z)$ is

$$\begin{cases} u(\mathbf{x}, t) = 2(10t + 1)(y - 0.5) \\ v(\mathbf{x}, t) = 2(10t + 1)(x - 0.5) \\ w(\mathbf{x}, t) = 0, \end{cases} \quad (6)$$

where t represents time, $t \in [0, 7]$. This simple field ensures a time-dependent velocity that increases linearly in time. The actual time between two consecutive outputs is 40ms and $x, y, z \in [0, 1]$. A boundary mesh, i.e., a cylinder, that matches the vortex, is also generated. The velocities at any position on the grid are known throughout time, and therefore are

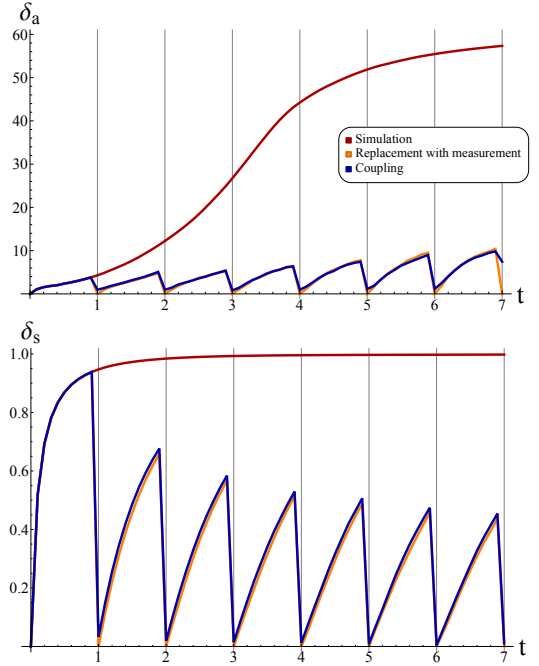


Figure 3: Comparison of the coupling with other simulation approaches using synthetic data. The field average of the per voxel speed and angle dissimilarity are presented. used as ground truth. Notice that linear interpolation in time will give a perfect result for this simple data set.

For all experiments, two dissimilarity measures are used for the comparison of the synthetic ground truth of an experiment with the computed velocity field. Let \mathbf{v} be the velocity field given by the ground truth and \mathbf{u} the estimated/computed velocity field. We define two measures for comparison of the three-directional velocity data: the relative dissimilarity in magnitude δ_s , and the angular dissimilarity measure, δ_a , i.e.,

$$\delta_s(\mathbf{x}) = \left| 1 - \frac{\|\mathbf{u}(\mathbf{x})\|}{\|\mathbf{v}(\mathbf{x})\|} \right| \quad (7)$$

$$\delta_a(\mathbf{x}) = \arccos \left(\frac{\mathbf{u}(\mathbf{x})}{\|\mathbf{u}(\mathbf{x})\|} \cdot \frac{\mathbf{v}(\mathbf{x})}{\|\mathbf{v}(\mathbf{x})\|} \right).$$

We separate the difference in speed and orientation, to get better understanding of the source of the differences. The ratio δ_s between the computed speed and the ground truth speed is such that 0 corresponds to $\|\mathbf{v}(\mathbf{x})\| = \|\mathbf{u}(\mathbf{x})\|$.

4.2. Coupling vs. Simulation

The first experiment compares the accuracy of the coupling method with that of pure simulation. It is important to note that the simulation cannot mimic the synthetic data, because the speed in these data increases over time. Instead, the simulation speed dampens out over time. Therefore, the simulation error is expected to increase. For the evaluation, the synthetic data computed using Eq. (6) will be used as measurement data. We compare the following approaches:

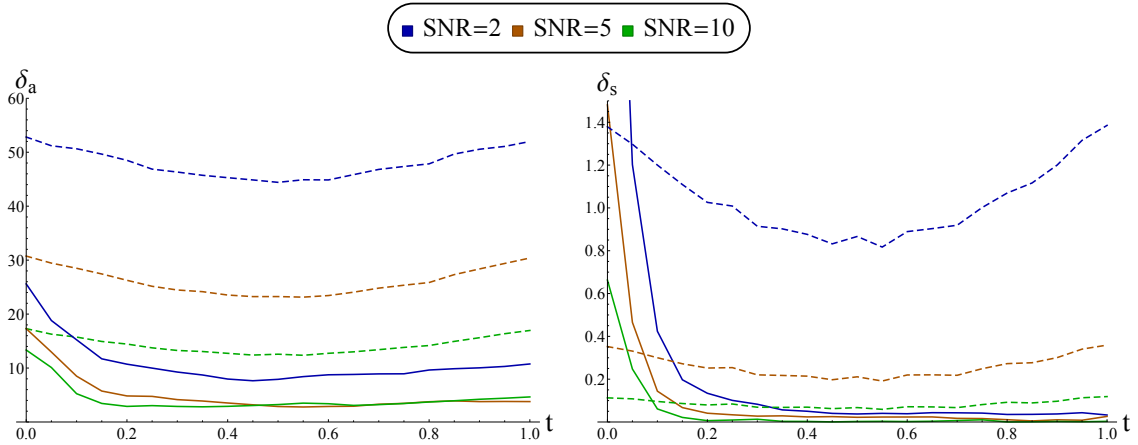


Figure 4: Comparison of the robustness to noise of the coupling method (solid lines) with the standard interpolation (dashed lines) using synthetic data. The average over the field of the per voxel speed and angle dissimilarity values for different SNR levels compared to the noiseless results are shown.

- Simulation: only the first measurement is used to initialize the simulation; the simulation will ensure that the flow field is divergence free.
- Replacement-with-measurement: replaces at each time frame the velocity of every simulation particle with the velocity of the measurement at the particle position. In this case, the ground truth is better fitted, but the results are not guaranteed to be physically correct.
- Coupling: our newly introduced method should approximate the measurement, and at the same time, it should guarantee a divergence-free flow field.

By definition, the replacement-with-measurement method is expected to give the lowest dissimilarity values, according to Eqs. (7). However, replacement-with-measurement produces a flow field that may not be physically correct, since the resulting flow may be compressible. Fig. 3 shows the average over the field of the per voxel speed and angle dissimilarity of the different methods. A new measurement is applied when time t has an integer value, as represented by the vertical lines. The dissimilarity is measured every 0.10 time steps. Fig. 3 shows that the coupling method, which ensures divergence-free flow, has an error close to the replacement-with-measurement method, which is the lowest possible.

4.3. Noise Robustness

MRI is subject to noise that influences the measurements, and results in uncertainty of the measured values. We expect that the coupling method, given noisy data, should produce more reproducible results than temporal linear interpolation. In this section, the robustness to noise of standard interpolation and coupling methods is evaluated.

The Rician noise of the PC-MRI methodology can be approximated by Gaussian noise [GP95]. For this experiment, different signal-to noise-ratios (SNRs) are used. The SNR is defined as $SNR = P_s/P_n$, where P_s and P_n denote signal and

noise power, respectively. P_s is given by the average velocity, whereas P_n can be set using the variance of the normal distribution [BHAA07]. Random values from a normal distribution are drawn using the Box-Muller approach.

For this experiment, two simulations are run, using noisy and noiseless data respectively. Both simulations are initialized with the previously-defined synthetic data. From this data, the set with the highest speed is selected to initialize the coupling method. The simulations are run and compared until $t = 1$. In Fig. 4, the per voxel average dissimilarity values using noiseless and noisy data are shown for different SNRs, namely 2, 5 and 10. Our measurements have an SNR of 10. As can be seen, in the coupling method the influence of noise is reduced. However, when more initial noise is added (i.e., $SNR = 2$), δ_a remains relatively high, compared to, e.g., the case with $SNR = 10$. The results using linear interpolation are also shown in Fig. 4 right. In this case, noise has been added at the two time steps, and standard linear interpolation has been applied for the positions in between. It can be observed that, in general, the robustness of the coupling method is clearly superior than that of interpolation. However, the coupling method is shown to be more sensitive to magnitude changes during the initial steps of the simulation when the influence of the measurements is the strongest.

5. Comparative Blood-Flow Visualization

In addition to the quantitative validation presented in the previous section, a qualitative assessment was carried out. Differences between the measurements and the coupled simulation are inspected using a dissimilarity measure, as well as tailor-made comparative visualizations.

We first inspect the dissimilarity measures at each time point of the blood-flow measurements. Fig. 5 depicts the dissimilarity measures, defined by Eqs. 7, using an oblique slice at peak systole. Analysis of the dissimilarity measures re-

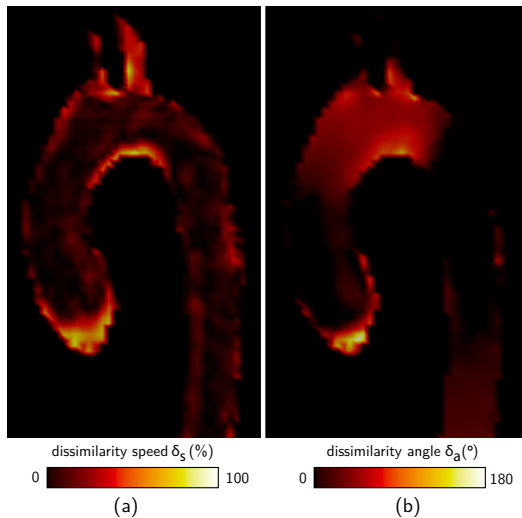


Figure 5: Results of the dissimilarity measures between the measured and coupled simulation velocities in an oblique slice. The slice is captured at peak systole for a healthy volunteer data set.

veals there are speed differences, in particular near the vessel wall. The overall speed, however, remains in the range of the measured velocity data. Angular differences occur in the top of the aortic arch, where the branching carotid arteries induce complex flow dynamics. The angular differences are, however, notably large near the vessel boundaries. Although for these data neither the measurement nor the coupled simulation can act as a ground truth, the initial exploration indicates that the coupled simulation adapts the measurement, and likely corrects the velocity field, especially near the vessel wall. These regions are known to be susceptible to acquisition artifacts, mainly due to motion caused by the cardiac contraction [PH93].

To further explore these differences near the vessel wall, we introduce a specific comparative visualization, as depicted in Fig. 6. Based on seed points near the vessel wall, arrows are used to represent the velocity vectors of the measurements and the coupled simulation. The seed points are positioned at the inside of the vessel boundary by translating the mesh vertices inwards along the surface normal with a fixed small offset, i.e., 0.5 mm. Subsequently, velocity vectors at a relatively small angle, determined by the dot product, are excluded from the visualization using a user-determined filtering threshold. The arrows that represent the measurement velocities are conveyed in gray, while for the simulation arrows the angle between velocity vectors is color-coded using the blackbody radiation color map. To visually maintain the spatial relations, the arrows are embedded in an anatomical context, comprising atoon-shaded vessel wall surface rendering with its front-faces culled.

Fig. 6 shows the comparative visualization of the velocity data at the aortic boundaries for a patient suffering from

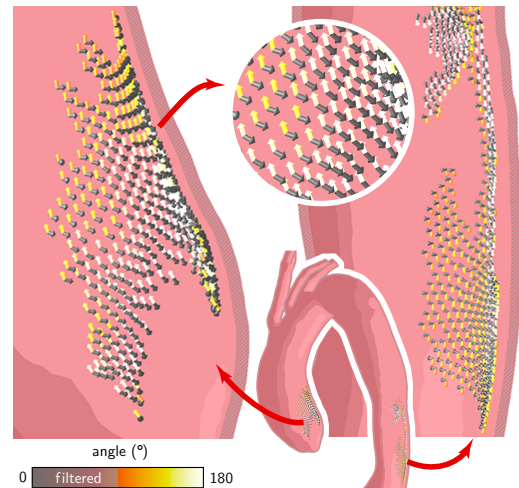


Figure 6: Measurement vectors are shown as gray arrows, and the coupled simulation vectors as arrows color-coded according to the angle between the vectors. Angles $> 90^\circ$ are depicted. The vectors are located close to the boundary at peak systole for an aortic dissection case.

an aortic dissection. Some regions reveal strong differences in the measured and simulated velocity vectors. Closer inspection shows that the gray measurement arrows occasionally point retrograde to main blood-flow direction. This is unlikely at peak systole, also for pathological flow, indicating corrected motion artifacts. The fluid simulation does not enforce specific hemodynamics, and there is no explicit notion of antegrade flow: if the fluid physics and anatomical boundaries dictate retrograde flow, the simulation will yield accordingly, and so will our coupled approach. In this specific case, the coupled simulation vectors at these locations convey credible hemodynamics, deemed consistent with the physiology. This substantiates our supposition that the coupled simulation is able to correct for acquisition artifacts near the vessel wall, based on the fluid physics.

Besides deviations near the boundary, we assess the differences between the full velocity fields using a comparative visualization based on integral lines. Therefore, we build on the work by Verma and Pang [VP04], which introduces a range of visualization approaches for flow data. In particular, we adopt the integral line comparison approach with a strip envelope.

Instead of streamlines, we compare pathlines that are randomly seeded throughout the aorta. At each seed position, two pathlines are generated for the duration of one time step in the measured data. The first pathline is traced in the measured velocity data, using Runge-Kutta 4 integration based on linear interpolation. The second pathline is based on the coupled simulation, traced in velocity data that is supersampled in time. The increased temporal resolution affects the

course of the simulation-based pathline, enabling comparison to conventional pathlines traced in measured data.

The pathlines are represented by tubes with an arrowhead to indicate the direction, as depicted in Fig. 7. Similar to the comparative visualization at the boundaries, the pathlines based on the measurements are depicted in gray. The pathlines based on the coupled simulation convey the distance between the two pathlines, using a black-body radiation color mapping based on the Hausdorff distance metric. Using a user-defined threshold, pathline sets with a small Hausdorff distance can be omitted from the visualization.

Fig. 7 shows that the gray pathlines, obtained from the measurement data, exhibit aberrant behavior near the vessel wall, due to the aforementioned acquisition artifacts. The zoom-in frames highlight two cases where the coupled simulation clearly adjusts the flow behavior, yielding more plausible pathlines. Furthermore, the surfaces between the pathlines clarify that there are substantial differences between the pathlines within the bloodstream. The adjustments applied by the coupled simulation to the individual velocity vectors rapidly accumulate to considerably different pathlines. Since pathline visualizations are the prevailing visualization technique for blood-flow analysis, it is essential that the used velocity fields yields valid pathline representations. Our coupled simulation contributes by enforcing fluid physics.

6. Discussion

To date, combinations of measurements and simulation for assessment of the hemodynamics are hardly investigated. Clinical practice relies mostly on imaging data for diagnosis and risk assessment, while biomedical research aims for understanding aided by blood-flow simulations. Physicians argue that measurements in the majority of the cases provide patient-specific information, and simulations are often too simplified to analyze patient-specific cases. Simulation researchers state that volumetric velocity measurements violate physical laws. We advocate for a combined measurement and simulations approach, with the intention to exploit the benefits of both and minimize their shortcomings. With our coupled simulation, we demonstrate that full measured velocity data can be integrated with simulation, enforcing fluid physics.

For the coupled simulation to converge, an appropriate initial condition is essential. Therefore, velocity data at time steps surrounding peak systole provide an adequate starting point. Noisy data with slow blood flow during early systole and throughout diastole will complicate convergence to a physically correct solution. Furthermore, the boundary conditions affect the results of the coupled simulation. The static manual segmentation of the vessel lumen best matches the bloodstream after the cardiac contraction during systole.

Our coupled simulation approach is implemented in the

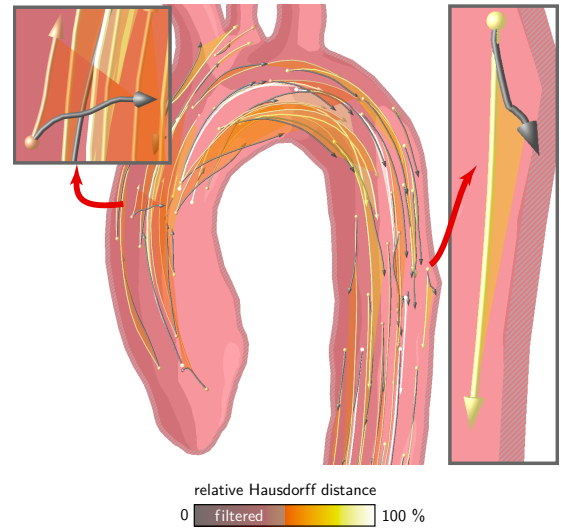


Figure 7: Comparative visualization of pathlines traced in the original measurements, depicted in gray, and the super-sampled velocity field obtained by our coupled simulation. The simulation pathlines are color-coded according to the Hausdorff distance. Pathlines with the 50% largest distances are depicted for a healthy volunteer data set at peak systole.

C++ programming language. For this, we extended the fluid solver by Batty et al. [BBB07] to support our coupling scheme; see also Bridson [Bri08] for additional implementation details regarding fluid simulations. For the involved linear algebra, we employ the LAPACK library [ABB*99]. Furthermore, the visualization is created using the OpenGL graphics library, and we exploit the capabilities of modern consumer hardware using the GLSL shading language.

The current implementation preprocesses the coupled simulation results, providing new 4D velocity field with an increased temporal resolution. Computation time is in the order of a few minutes per time step of the measured data, depending on simulation grid size, the number of particles, and the complexity of the fluid behavior. Many fluid simulations in the computer graphics research field, however, have been shown to perform in real-time on modern consumer graphics hardware, including the FLIP method we have adopted [HG09]. In contrast to CFD approaches, this provides great potential to perform a real-time coupling approach in new blood-flow visualization techniques.

Finally, work is in progress to extend our coupling method such that it also considers viscous effects. To achieve this, we included the additional viscosity term $\mu \nabla^2 \mathbf{u} / \rho$ to the right-hand-side of Eq. (1), with μ the dynamic (blood) viscosity. Similarly, the term $\mu \nabla \cdot (\nabla \mathbf{u}_m + (\nabla \mathbf{u}_m)^T) / \rho$ was included in Eq. (4), since we assume that the densities are identical and the measured velocity may not be incompressible, so that $\nabla \cdot (\nabla \mathbf{u}_m)^T \neq 0$. We then use the ‘no-slip’ boundary condition and the implicit viscosity solver by Batty and Brid-

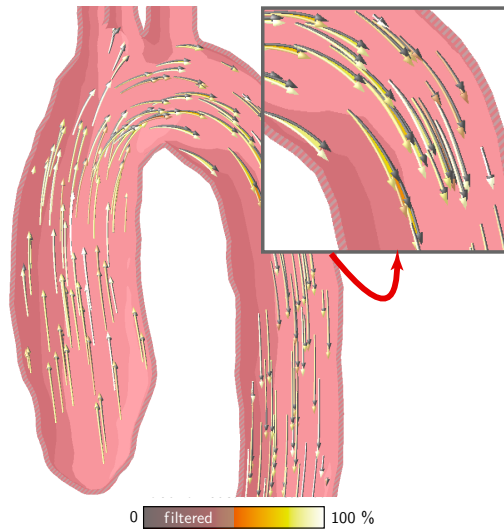


Figure 8: Comparative visualization between inviscid (gray pathlines) and viscid (pathlines color-coded by the Hausdorff distance) simulation velocities. In both cases, our measurement-simulation coupling scheme was used. Only the pathlines with the 50% largest distances are shown.

son [BB08]. The result of a preliminary experiment, comparing inviscid and viscid simulation velocities, are shown in Fig. 8. In both cases, the simulation velocities were coupled to velocity measurements. As can be seen, the differences in orientation and magnitude between the two velocity sets are small. In our experiments, we could also observe that the differences are larger close to the vessel walls, where viscous effects are expected to be larger. Those initial experiments indicate that there are differences, and therefore the viscous model is preferable, since theoretically, it better represents physical reality.

7. Conclusions and Future work

Blood-flow velocity measurements are prone to acquisition artifacts, while fluid simulations rely on uncertain model assumptions. We advocate a combined approach, harnessing the benefits of both measurements and simulations, improving the visual analysis of hemodynamics. We have demonstrated a coupled fluid simulation approach that emanates from the full 4D PC-MRI blood-flow velocity data, while imposing physical properties of the hemodynamics. Based on the difference between the velocity fields of the measurement and simulation, the coupled simulation yields physically underpinned velocity data between the time steps of the MRI data, addressing the coarse temporal resolution of the measurements. Moreover, acquisition artifacts, in particular near the vessel wall, are corrected by the coupled simulation.

The proposed coupling method has been evaluated using synthetic data, investigating the accuracy and robustness to

noise. The results indicate that the coupling method is more robust to noise than the standard interpolation method. However, further validation, e.g., using a physical phantom, is necessary to provide solid conclusions. Such validation is out of the scope of this paper, but essential to prove the validity of the approach for clinical applications.

Visual assessment using the coupled simulation with 4D PC-MRI data showed that the largest differences are found near the vessel wall. The comparative boundary visualization revealed areas with strong angular differences between the measurements and the coupled simulations, where the adjusted velocity vectors of the simulation are in line with the known direction of the bloodstream. This inspires confidence in the physical underpinning of the coupled simulation. Further analysis with our comparative pathline visualization confirms this correcting behavior near the vessel walls. Furthermore, this visualization shows that the pathline sets within the blood flow differ substantially, which is due to the line traces that accumulate the relatively small adjustments applied to the velocity field. This motivates the need for a combined approach to obtain the best possible velocity field as a basis for a pathline visualization.

In the future, the accuracy of the coupling method would benefit from a less restrictive boundary condition that is time-varying [HK04]. The numerics of the main simulation algorithm can be improved, along with the coupling scheme: the user should be allowed more control over coupling by using a weighting function $\gamma(\mathbf{x}, t)$ that prioritizes either measurement or simulation in certain regions of the simulation grid. The coupled approach currently includes measurement data while the simulation advances forward. Another conceivable direction would be to have a predictive coupling approach, which takes into account the measured time steps that are available after the current simulation time.

On the longer term, the coupled approach could be used to provide prognostic information for treatment planning. Influence on the hemodynamics can be inspected for different morphological changes, or for different intervention schemes, such as stent or prosthetic valve placement. Also, the benefit of the proposed method for other domains outside 4D PC-MRI can be explored, e.g., meteorology.

To the best of our knowledge, we presented the first method that combines full 4D PC-MRI velocity data with fluid simulation. We underpinned the value of such a coupled approach, and encourage future research in this direction.

Acknowledgments

We would like to thank prof. F.N. van de Vosse from the Cardiovascular Biomechanics group at Eindhoven University of Technology for sharing his knowledge and expertise in the area of physical modeling of hemodynamics.

References

- [ABB*99] ANDERSON E., BAI Z., BISCHOF C., BLACKFORD S., DEMMEL J., DONGARRA J., DU CROZ J., GREENBAUM A., HAMMARLING S., MCKENNEY A., SORENSEN D.: *LAPACK Users' Guide*, third ed. Society for Industrial and Applied Mathematics, 1999. 8
- [BB08] BATTY C., BRIDSON R.: Accurate viscous free surfaces for buckling, coiling, and rotating liquids. In *ACM SIGGRAPH/Eurographics Symposium on Computer Animation* (2008), pp. 219–228. 9
- [BBB07] BATTY C., BERTAILS F., BRIDSON R.: A fast variational framework for accurate solid-fluid coupling. *ACM Transactions on Graphics* 26, 3 (2007), 100:1–100:7. 4, 5, 8
- [BHAA07] BAMMER R., HOPE T., AKSOY M., ALLEY M.: Time-resolved 3D quantitative flow MRI of the major intracranial vessels: Initial experience and comparative evaluation at 1.5T and 3.0T in combination with parallel imaging. *Magnetic Resonance in Medicine* 57, 1 (2007), 127–140. 6
- [BKR88] BRACKBILL J., KOTHE D., RUPPEL H.: FLIP: A low-dissipation, particle-in-cell method for fluid flow. *Computer Physics Communications* 48, 1 (1988), 25–38. 3, 4
- [BMGS13] BORN S., MARKL M., GUTBERLET M., SCHEUERMANN G.: Illustrative visualization of cardiac and aortic blood flow from 4D MRI data. In *IEEE Pacific Visualization* (2013), pp. 129–136. 2
- [Bri08] BRIDSON R.: *Fluid Simulation for Computer Graphics*. A.K. Peters, 2008. 3, 8
- [DPV12] D'ELIA M., PEREGO M., VENEZIANI A.: A variational data assimilation procedure for the incompressible navier-stokes equations in hemodynamics. *Journal of Scientific Computing* 52, 2 (2012), 340–359. 3
- [FHS*05] FUNAMOTO K., HAYASE T., SHIRAI A., SAIJO Y., YAMBE T.: Fundamental study of ultrasonic-measurement-integrated simulation of real blood flow in the aorta. *Annals of Biomedical Engineering* 33, 4 (2005), 415–428. 3
- [FM97] FOSTER N., METAXAS D.: Controlling fluid animation. In *Computer Graphics International* (1997), pp. 178–188. 3
- [GM77] GINGOLD R. A., MONAGHAN J. J.: Smoothed particle hydrodynamics: theory and application to non-spherical stars. *Monthly Notices of the Royal Astronomical Society* 181 (1977), 375–389. 4
- [GMR91] GHIL M., MALANOTTE-RIZZOLI P.: Data assimilation in meteorology and oceanography. *Advances in Geophysics* 33 (1991), 141–266. 2
- [GMR*13] GO A. S., MOZAFFARIAN D., ROGER V. L., BENJAMIN E. J., BERRY J. D., BORDEN W. B., BRAVATA D. M., DAI S., FORD E. S., FOX C. S., FRANCO S., FULLERTON H. J., GILLESPIE C., HAILPERN S. M., HEIT J. A., HOWARD V. J., HUFFMAN M. D., KISSELA B. M., KITNER S. J., LACKLAND D. T., LICHTMAN J. H., LISABETH L. D., MAGID D., MARCUS G. M., MARELLI A., MATCHAR D. B., MCGUIRE D. K., MOHLER E. R., MOY C. S., MUSSOLINO M. E., NICHOL G., PAYNTER N. P., SCHREINER P. J., SORLIE P. D., J. STEIN T. N. T., VIRANI S. S., WONG N. D., WOO D., TURNER M. B.: Heart disease and stroke statistics - 2013 update. *Circulation* 127, 1 (2013), e6–e245. 1
- [GP95] GUDBJARTSSON H., PATZ S.: The Rician distribution of noisy MRI data. *Magnetic Resonance in Medicine* 34, 6 (1995), 910–914. 6
- [GWV*02] GLOR F. P., WESTENBERG J. J. M., VIERENDEELS J., DANILOUCHKINE M., VERDONCK P.: Validation of the coupling of magnetic resonance imaging velocity measurements with computational fluid dynamics in a U bend. *Artificial Organs* 26, 7 (2002), 622–35. 3
- [HG09] HORVATH C., GEIGER W.: Directable, high-resolution simulation of fire on the GPU. *ACM Transactions on Graphics* 28, 3 (2009), 41:1–41:8. 8
- [HK04] HONG J.-M., KIM C.-H.: Controlling fluid animation with geometric potential. *Computer Animation and Virtual Worlds* 15, 3–4 (2004), 147–157. 3, 9
- [KGP*13] KÖHLER B., GASTEIGER R., PREIM U., THEISEL H., GUTBERLET M., PREIM B.: Semi-Automatic vortex extraction in 4D PC-MRI cardiac blood flow data using line predicates. *IEEE Transactions on Visualization and Computer Graphics* 19, 12 (2013), 2773–2783. 2
- [MCG03] MÜLLER M., CHARYPAR D., GROSS M.: Particle-based fluid simulations for interactive applications. In *ACM SIGGRAPH/Eurographics Symposium on Computer Animation* (2003), pp. 154–159. 3
- [MFK*12] MARKL M., FRYDRYCHOWICZ A., KOZERKE S., HOPE M., WIEBEN O.: 4D flow MRI. *Journal of Magnetic Resonance Imaging* 36, 5 (2012), 1015–1036. 1, 2
- [PH93] POTCHEN E. J., HAACKE E. M.: *Magnetic resonance angiography: concepts & applications*. Mosby-Year Book, 1993. 7
- [SHFF11] SCHWENKE M., HENNEMUTH A., FISCHER B., FRIMAN O.: Blood flow computation in phase-contrast MRI by minimal paths in anisotropic media. *Medical Image Computing and Computer-Assisted Intervention* 14, 1 (2011), 436–443. 2
- [SRF05] SELLE A., RASMUSSEN N., FEDKIW R.: A vortex particle method for smoke, water and explosions. *ACM Transactions on Graphics* 24, 3 (2005), 910–914. 3
- [Sta99] STAM J.: Stable fluids. In *SIGGRAPH Proceedings of the Conference on Computer Graphics and Interactive Techniques* (1999), pp. 121–128. 2
- [TF09] TAYLOR C. A., FIGUEROA C. A.: Patient-specific modeling of cardiovascular mechanics. *Annual Review of Biomedical Engineering* 11 (2009), 109–34. 2
- [THZ98] TAYLOR C. A., HUGHES T., ZARINS C.: Finite element modeling of blood flow in arteries. *Computer Methods in Applied Mechanical Engineering* 7825, 97 (1998), 155–196. 5
- [VP04] VERMA V., PANG A.: Comparative flow visualization. *IEEE Transactions on Visualization and Computer Graphics* 10, 6 (2004), 609–24. 7
- [VPvP*12] VILANOVA A., PREIM B., VAN PELT R., GASTEIGER R., NEUGEBAUER M., WISCHGOLL T.: Visual exploration of simulated and measured blood flow. *Computing Research Repository - arXiv abs/1209.0999* (2012). URL: <http://arxiv.org/abs/1209.0999>. 2
- [WWK*01] WOOD N. B., WESTON S. J., KILNER P. J., GOSMAN A. D., FIRMIN D. N.: Combined MR imaging and CFD simulation of flow in the human descending aorta. *Journal of Magnetic Resonance Imaging* 13, 5 (2001), 699–713. 3
- [ZB05] ZHU Y., BRIDSON R.: Animating sand as a fluid. *ACM Transactions on Graphics* 24, 3 (2005), 965–972. 4
- [Zha05] ZHAO H.: A fast sweeping method for Eikonal equations. *Mathematics of Computation* 74 (2005), 603–627. 4